

# The mass function of dark matter haloes

A. Jenkins,<sup>1</sup>\* C. S. Frenk,<sup>1</sup> S. D. M. White,<sup>2</sup> J. M. Colberg,<sup>2</sup> S. Cole,<sup>1</sup> A. E. Evrard,<sup>3</sup>  
H. M. P. Couchman<sup>4</sup> and N. Yoshida<sup>2</sup>

<sup>1</sup>*Department of Physics, University of Durham, South Road, Durham, DH1 3LE*

<sup>2</sup>*Max-Planck-Institut für Astrophysik, Garching, D-85740 München, Germany*

<sup>3</sup>*Department of Physics, University of Michigan, Ann Arbor, MI 48109-1120, USA*

<sup>4</sup>*Department of Physics and Astronomy, McMaster University, Hamilton, Ontario L8S 4M1, Canada*

Accepted 2000 September 11. Received 2000 August 18; in original form 2000 May 10

## ABSTRACT

We combine data from a number of  $N$ -body simulations to predict the abundance of dark haloes in cold dark matter (CDM) universes over more than four orders of magnitude in mass. A comparison of different simulations suggests that the dominant uncertainty in our results is systematic and is smaller than 10–30 per cent at all masses, depending on the halo definition used. In particular, our ‘Hubble volume’ simulations of  $\tau$ CDM and  $\Lambda$ CDM cosmologies allow the abundance of massive clusters to be predicted with uncertainties well below those expected in all currently planned observational surveys. We show that for a range of CDM cosmologies and for a suitable halo definition, the simulated mass function is almost independent of epoch, of cosmological parameters and of the initial power spectrum when expressed in appropriate variables. This universality is of exactly the kind predicted by the familiar Press–Schechter model, although this model predicts a mass function shape that differs from our numerical results, overestimating the abundance of ‘typical’ haloes and underestimating that of massive systems.

**Key words:** gravitation – methods: numerical – cosmology: theory – dark matter.

## 1 INTRODUCTION

Accurate theoretical predictions for halo mass functions are needed for a number of reasons. For example, they are a primary input for modelling galaxy formation, since current theories assume galaxies to result from the condensation of gas in halo cores (White & Rees 1978, and many subsequent papers; see Somerville & Primack 1999 for a recent overview). The abundance of the most massive haloes is sensitive to the overall amplitude of mass fluctuations, while the evolution of this abundance is sensitive to the cosmological density parameter,  $\Omega_0$ . As a result, identifying massive haloes with rich galaxy clusters can provide an estimate both of the amplitude of the primordial density fluctuations and of the value of  $\Omega_0$ ; recent discussions include Henry (1997), Eke et al. (1998), Bahcall & Fan (1998), Blanchard & Bartlett (1998) and the Virgo consortium presentation of the Hubble volume simulations used below (Evrard et al. 2000). The mass function is also a critical ingredient in the apparently strong constraints on cosmological parameters (principally  $\Omega_0$  and  $\Lambda$ ) which can be derived from the observed incidence of strong gravitational lensing (e.g. Bartelmann et al. 1998; Falco, Kochanek & Munoz 1998).

As the observational data relevant to these issues improve, the

need for accurate theoretical predictions increases. By far the most widely used analytic formulae for halo mass functions are based on extensions of the theoretical framework first sketched by Press & Schechter (1974). Unfortunately, none of these derivations is sufficiently rigorous that the resulting formulae can be considered accurate beyond the regime where they have been tested against  $N$ -body simulations. In this paper, we combine mass functions from simulations of four popular versions of the cold dark matter (CDM) cosmology to obtain results valid over a wider mass range and to higher accuracy than has been possible before. These mass functions show a regularity that allows them all to be fitted by a single interpolation formula despite the wide range of epochs and masses that they cover. This formula can be used to obtain accurate predictions for CDM models with parameters other than those we have simulated explicitly.

Although the analytical framework of the Press–Schechter (PS) model has been greatly refined and extended in recent years, in particular to allow predictions for the merger histories of dark matter haloes (Bond et al. 1991; Bower 1991; Lacey & Cole 1993), it is well known that the PS mass function, while qualitatively correct, disagrees in detail with the results of  $N$ -body simulations. Specifically, the PS formula overestimates the abundance of haloes near the characteristic mass  $M_*$  and underestimates the abundance in the high-mass tail (Efstathiou & Rees 1988; Efstathiou et al. 1988; White, Efstathiou & Frenk 1993;

\* E-mail: A.R.Jenkins@durham.ac.uk

Lacey & Cole 1994; Eke, Cole & Frenk 1996; Gross et al. 1998; Governato et al. 1999). Recent work has studied whether this discrepancy can be resolved by replacing the spherical collapse model of the standard PS analysis by ellipsoidal collapse (e.g. Monaco 1997a,b; Lee & Shandarin 1998; Sheth, Mo & Tormen 1999). Sheth et al. (1999) were able to show that this replacement plausibly leads to a mass function almost identical to that which Sheth & Tormen (1999) had earlier fitted to a subset of the numerical data we analyse below. Note that at present there is no good numerical test of analytic predictions for the low-mass tail of the mass function, and our analysis in this paper does not remedy this situation.

Several authors have considered halo mass functions in models with scale-free Gaussian initial fluctuations. The attraction is that clustering should be self-similar in time in such models when  $\Omega = 1$ . This expectation is easy to test numerically and appears substantiated by the available simulation data (Efstathiou et al. 1988; Lacey & Cole 1994). Deviations from self-similarity can be used to isolate numerical artefacts that break the scaling. The CDM power spectrum is not scale-free although the variation of the effective spectral index with wavenumber is gentle. Recently, a number of very large CDM simulations have been performed by Gross et al. (1998) and Governato et al. (1999). These confirmed the deviations from the PS prediction found in earlier work and extended coverage to both higher and lower masses. An interesting question is how the non-power-law nature of the fluctuation spectrum affects the mass function. PS theory predicts there to be no effect when the mass function is expressed in suitable variables. However, Governato et al. (1999) find evidence that the high-mass deviation from the PS prediction increases with increasing redshift, although the effect is small.

The essence of group finding is to convert a discrete representation of a continuous density field into a countable set of ‘objects’. In general, this conversion is affected both by the degree of discreteness in the realization (the particle mass) and by the detailed characteristics of the object definition algorithm. The definition of object boundaries is somewhat arbitrary, and one can expect the characteristics of the object set to vary according to the specific assumptions adopted. This introduces uncertainties when comparing simulations and analytic models. We examine here two of the standard algorithms used in earlier literature, the friends-of-friends and spherical overdensity group finders (Davis et al. 1985; Lacey & Cole 1994). Motivated by spherical collapse models, both attempt to identify virialized regions that are overdense by a factor  $\sim 200$  with respect to the global mean. Some comparisons

of these algorithms have already been published by Lacey & Cole (1994) who found small but measurable differences.

In reality, haloes possess a variety of physical characteristics that can be employed by observers to form new, and possibly different, countable sets. For example, the Coma cluster is a single object to an X-ray observer but contains hundreds of visible galaxies. Similarly, very high-resolution simulations reveal a myriad of smaller, self-bound ‘sub-haloes’ within the virial region of each parent halo (e.g. Moore et al. 1999; Klypin et al. 1999). The distinction between the larger halo and its substructure is largely one of density: the sub-haloes are bounded at a much higher density than the parent object. Such subtleties further complicate comparisons between theory, experiment and observation, and in all such analysis it is important to take careful account of the specific algorithms used to define the objects considered.

In Section 2, we describe the simulations and the two halo finders that we employ when determining halo mass functions. In Section 3, we investigate the consistency of the mass functions derived from different simulations of the  $\tau$ CDM and  $\Lambda$ CDM cosmologies. In Section 4, we present our results for the  $\tau$ CDM and  $\Lambda$ CDM models and compare them with PS theory and with the Sheth–Tormen fitting formula. In Section 5, we examine the evolution of the high-mass end of the mass function with redshift. Using the insight that this provides, we generalize our results and show that, if a single linking length is used to define haloes, then a single fitting formula, very close to that proposed by Sheth & Tormen, accurately describes the mass functions in  $\tau$ CDM,  $\Lambda$ CDM, SCDM and OCDM models over a wide range of redshifts. We present and discuss our conclusions in Section 6, where we also explain how to obtain some of the simulation data and the analysis software used in our study. Appendix A tests the influence of numerical parameters on our measured mass functions, while Appendix B gives ‘best-fitting’ analytic representations of a number of our mass functions.

## 2 SIMULATION DETAILS

### 2.1 The simulations

For the main analysis of this paper we measure halo mass functions in a number of  $N$ -body simulations carried out by the Virgo consortium for two cosmological models,  $\tau$ CDM and  $\Lambda$ CDM, as introduced by Jenkins et al. (1998). The simulation parameters are listed in Table 1. The largest calculations are the two ‘Hubble volume’ simulations, each with  $10^9$  particles in boxes

**Table 1.**  $N$ -body simulation parameters.

Run	$\Omega_0$	$\Lambda_0$	$\Gamma$	$\sigma_8$	$N_{\text{part}}$	$L_{\text{box}} (h^{-1} \text{Mpc})$	$m_{\text{part}} (h^{-1} M_{\odot})$	$r_{\text{soft}} (h^{-1} \text{kpc})$
$\tau$ CDM-gif	1.0	0.0	0.21	0.60	16 777 216	84.5	$1.00 \times 10^{10}$	30
$\tau$ CDM-int	1.0	0.0	0.21	0.60	16 777 216	160.3	$6.82 \times 10^{10}$	10
$\tau$ CDM-512	1.0	0.0	0.21	0.51	134 217 728	320.7	$6.82 \times 10^{10}$	30
$\tau$ CDM-virgo	1.0	0.0	0.21	0.60	16 777 216	239.5	$2.27 \times 10^{11}$	30
$\tau$ CDM-hub	1.0	0.0	0.21	0.60	1000 000 000	2000.0	$2.22 \times 10^{12}$	100
$\Lambda$ CDM-gif	0.3	0.7	0.21	0.90	16 777 216	141.3	$1.40 \times 10^{10}$	25
$\Lambda$ CDM-512	0.3	0.7	0.21	0.90	134 217 728	479.0	$6.82 \times 10^{10}$	30
$\Lambda$ CDM-hub	0.3	0.7	0.21	0.90	1000 000 000	3000.0	$2.25 \times 10^{12}$	100
$\tau$ CDM-test1	1.0	0.0	0.21	0.60	1000 000	200.0	$2.22 \times 10^{12}$	100
$\tau$ CDM-test2	1.0	0.0	0.21	0.60	1000 000	200.0	$2.22 \times 10^{12}$	30
$\tau$ CDM-test3	1.0	0.0	0.21	0.60	8000 000	200.0	$2.77 \times 10^{11}$	100

of volume 8 and  $27 h^{-3} \text{Gpc}^3$  respectively. [We express the Hubble constant as  $H_0 = 100 h \text{km s}^{-1} \text{Mpc}^{-1}$ .] These simulations allow the mass function to be determined for very massive clusters ( $> 10^{15} h^{-1} M_\odot$ ) with relatively small Poisson errors. In addition, we have analysed several simulations of smaller volumes, but with better mass resolution, from which the mass function can be determined reliably down to masses of a few times  $10^{11} M_\odot$ . In Section 5 we also include data from the large  $\Lambda$ CDM simulations carried out by Governato et al. (1999) and from the simulations of  $\Lambda$ CDM and OCDM discussed in Jenkins et al. (1998).

The models listed in Table 1 are all normalized so as to be consistent with the observed local abundance of rich galaxy clusters (White et al. 1993; Eke et al. 1996; Viana & Liddle 1996) and are also consistent with the standard *COBE* normalization (e.g. Ratra et al. 1997). However, for the most part, the precise normalization is unimportant for the purposes of this paper. The power spectrum of the initial conditions of all the simulations except  $\Lambda$ CDM-hub and  $\Lambda$ CDM-512 was set up using the transfer function given by Bond & Efstathiou (1984),

$$T(k) = \frac{1}{\{1 + [aq + (bq)^{3/2} + (cq)^2]^\nu\}^{1/\nu}}, \quad (1)$$

where  $q = k/\Gamma$ ,  $a = 6.4 h^{-1} \text{Mpc}$ ,  $b = 3 h^{-1} \text{Mpc}$ ,  $c = 1.7 h^{-1} \text{Mpc}$  and  $\nu = 1.13$ . For the  $\Lambda$ CDM-hub and  $\Lambda$ CDM-512 simulations, the transfer function was computed using *CMBFAST* (Seljak & Zaldarriaga 1996), assuming  $h = 0.7$  and  $\Omega_{\text{baryon}} h^2 = 0.0196$  (Burles & Tytler 1998). In all models, the slope of the primordial power spectrum was taken to be unity. Full details of how the simulations were set up are given in Jenkins et al. (1998), for simulations ending in -gif, -int, -virgo and -test, and in Evrard et al. (2000), for simulations ending in -hub. More recently, we have completed 512<sup>3</sup>-particle simulations of the  $\tau$ CDM and  $\Lambda$ CDM models using essentially the same code that we used for the Hubble volume calculations.

Each simulation yields a determination of the mass function over a mass range dictated by the particle mass and the number of particles in the simulation. To aid understanding, we have performed a set of smaller test simulations (see bottom of Table 1), designed to investigate the sensitivity of the mass function to changes in a single numerical parameter at a time. The parameters that we vary are the particle mass, the gravitational softening and the starting redshift. These checks (discussed in Appendix A) also give an indication of the number of particles required to determine the mass function satisfactorily using different halo finders.

## 2.2 Halo finders

We use two different algorithms to identify dark matter haloes: the friends-of-friends (FOF) algorithm of Davis et al. (1985), and the spherical overdensity (SO) finder described by Lacey & Cole (1994).

The FOF halo finder depends on just one parameter,  $b$ , which defines the linking length as  $bn^{-1/3}$  where  $n$  is the mean particle density. An attractive feature of the FOF method is that it does not impose any fixed shape on the haloes. A disadvantage is that it may occasionally link two haloes accidentally through a chance bridge of particles. In the limit of very large numbers of particles per object, FOF approximately selects the matter enclosed by an isodensity contour  $\alpha 1/b^3$ .

In the SO algorithm, the mass of a halo is evaluated in a spherical region. There is one free parameter, the mean overdensity,

$\kappa$ , of the haloes. There are many possible ways of centring the spherical region. In our case, the centre is determined iteratively, after making an initial guess based on an estimate of the local density for each particle, recentring on the centre of mass, growing a sphere outwards about the new centre until it reaches the desired mean overdensity, and recomputing the centre of mass. After several iterations, the motion of the centre becomes small. An alternative method consists of centring the sphere on the local maximum enclosed mass at fixed overdensity, but this is more computationally intensive – a strong disincentive when identifying SO groups in the Hubble volume simulations.

The conventional choices for  $\Omega = 1$  cosmologies are FOF ( $b = 0.2$ ) and SO( $\kappa = 180$ ) (Davis et al. 1985; Lacey & Cole 1994). For models where  $\Omega \neq 1$ , the choice is less obvious. At late times, groups stop growing and the appropriate linking length or bounding density should plausibly become constant in physical coordinates. At early times  $\Omega \approx 1$ , and it is the corresponding comoving quantities that are most naturally kept fixed. One needs to decide how to make the transition between these two regimes. Lacey & Cole (1994) and Eke et al. (1996) have done this using the spherical top-hat collapse model. We adopt their approach for the analysis in Section 4, taking FOF( $b = 0.164$ ) and SO( $\kappa = 32$ ) for  $\Lambda$ CDM at  $z = 0$ . This choice cannot be rigorously justified, however, and we find in Section 5 that simpler results are obtained by using the conventional Einstein–de Sitter parameters also for this cosmology and for OCDM.

## 3 CONSISTENCY CHECKS

It is important to check the reliability of mass functions determined from simulations. From a formal point of view this is impossible, since there is no known analytic solution for any realistic halo definition. It is, however, possible to check for consistency between different simulations and different halo definitions. The mass ranges covered by the different simulations in each of our sets overlap considerably. As we show below, the agreement in these overlap regions is far from perfect. One source of difference is just the Poisson error due to the finite number of clusters in each simulation. In the following we will only use numerical data for which such Poisson errors are below 10 per cent and are negligible compared to systematic errors. These, we attribute to weak dependences of the measured mass functions on some of the numerical parameters of our simulations. Such systematics appear to be smaller than about 10 per cent for the FOF halo finder and about 30 per cent for the SO halo finder, and are therefore too small to be a major concern. It seems unlikely that observational determinations of halo mass functions will reduce systematic uncertainties to such small levels in the foreseeable future.

Defining  $n(M)$  to be the number of haloes with mass less than  $M$ , we plot the differential mass functions,  $dn/d \ln M$  for all  $\tau$ CDM simulations in Table 1 with  $\sigma_8 = 0.6$  and for all  $\Lambda$ CDM simulations with  $\sigma_8 = 0.9$ , excluding the last three test simulations. The mass functions for the test simulations are plotted in Appendix A and compared with other simulations to show how much the mass function can vary as a result of changes in the particle mass, gravitational softening and starting redshift.

The FOF mass functions for our two cosmologies are displayed in Fig. 1. The numerical data have been smoothed with a kernel that is Gaussian in  $\log_{10}(M)$  with rms width 0.08. This smoothing erases high-frequency Poisson noise and provides a continuous

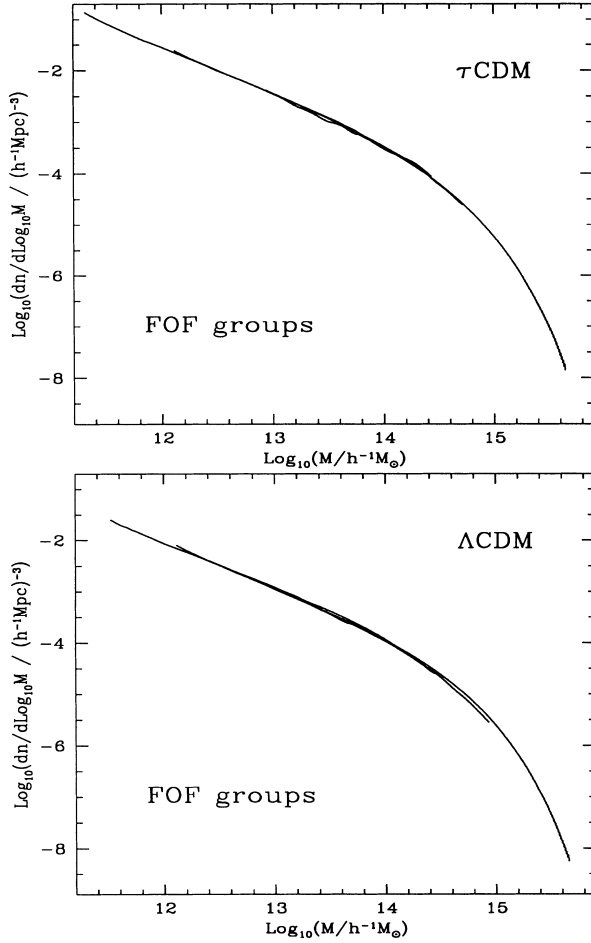


**Figure 1.** Friends-of-friends differential mass functions for dark matter haloes in the  $\tau$ CDM and  $\Lambda$ CDM simulations. Haloes were identified using linking lengths of 0.2 and 0.164 respectively. The different curves correspond to the various simulations detailed in Table 1. The mass resolution in the simulations varies by more than two orders of magnitude and the volume surveyed by more than four orders of magnitude. In all cases, the mass functions are truncated at the low-mass end at the mass corresponding to 20 particles, and at the high-mass end at the point where the predicted Poisson abundance errors reach 10 per cent. The simulations match up very well.

curve for comparison with analytic predictions. Using a ‘bin’ shape without sharp edges also reduces fluctuations at the low-mass end where the halo masses are integer multiples of the particle mass. For a power-law mass function,  $F \equiv dn/d\log_{10}M \propto M^{-\alpha}$ , such smoothing raises the amplitude by approximately  $\exp(\alpha^2/59)$ . For the  $\tau$ CDM mass function, this factor is about 1.03 at  $10^{14} h^{-1} M_{\odot}$ , 1.14 at  $10^{15} h^{-1} M_{\odot}$  and 1.7 at the highest masses we plot; similar numbers apply to  $\Lambda$ CDM. Poisson statistics lead to rms uncertainties in the smoothed curves which are

$$\frac{\delta F_{\text{rms}}}{F} \approx 1.88 \left( V_{\text{sim}} \frac{dn}{d\log_{10} M} \right)^{-1/2} \exp(-\alpha^2/79), \quad (2)$$

where  $V_{\text{sim}}$  is the volume of the simulation considered and errors are correlated over a distance comparable to the smoothing length-scale. As noted above, we only plot curves for which this uncertainty is below 10 per cent and is small compared to other sources of error.

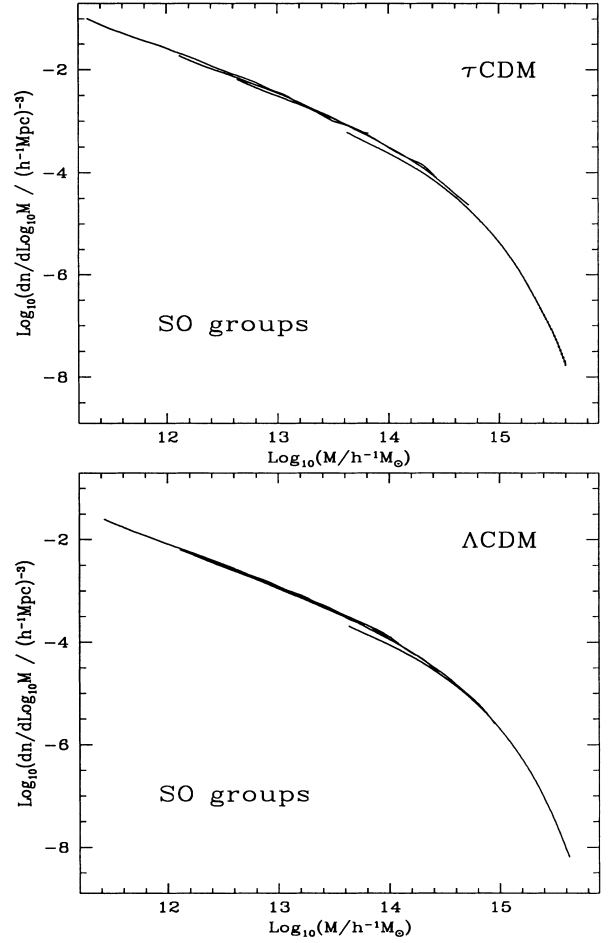


**Figure 2.** Spherical overdensity differential mass function for dark haloes in the  $\tau$ CDM and  $\Lambda$ CDM simulations. Halo masses were defined at mean interior overdensities of 180 and 324 respectively. The different curves correspond to the various simulations detailed in Table 1 and are truncated as in Fig. 1. The simulations do not match up as well here as in Fig. 1. Simulations with coarse mass resolution seem to underestimate the halo abundance near their lower mass limit. See the text for further details.

As can be seen in Fig. 1, FOF mass functions for different simulations match well even when the number of particles per halo is small. The linking parameter was taken to be  $b = 0.2$  for  $\tau$ CDM and  $b = 0.164$  for  $\Lambda$ CDM. For the smaller boxes, Poisson fluctuations are clearly visible at the high-mass end of the plotted curves. Such fluctuations are much less pronounced in the curves derived from the Hubble volume simulations, because the mass function is then much steeper at the point where discreteness noise becomes appreciable and our smoothing erases features more efficiently.

Fig. 2 shows a similar comparison of mass functions obtained using the SO halo finder. The mean overdensity was set to 180 and 324 in the  $\tau$ CDM and  $\Lambda$ CDM cases respectively. Here we see a systematic effect: the abundance at given halo mass in a simulation with large particle mass is always lower than that found in a simulation with smaller particle mass. The difference is particularly pronounced between the Hubble volume simulations and the others, but this merely continues a trend of increasing discrepancy as the halo mass at the matching point becomes larger. The tests carried out in Appendix A show that these mismatches result from resolution effects on halo structure, which particularly

affect haloes identified with the SO algorithm. Robust results require a minimum of about 100 particles per SO halo, but only a minimum of about 20 particles per FOF halo.

#### 4 COMPARISON WITH ANALYTIC MODELS

In this section, we compare some popular analytic models to the mass functions constructed above. It proves convenient to use the quantity  $\ln \sigma^{-1}(M, z)$  as the mass variable instead of  $M$ , where  $\sigma^2(M, z)$  is the variance of the linear density field, extrapolated to the redshift  $z$  at which haloes are identified, after smoothing with a spherical top-hat filter which encloses mass  $M$  in the mean. This variance can be expressed in terms of the power spectrum  $P(k)$  of the linear density field extrapolated to redshift zero as:

$$\sigma^2(M, z) = \frac{b^2(z)}{2\pi^2} \int_0^\infty k^2 P(k) W^2(k; M) dk, \quad (3)$$

where  $b(z)$  is the growth factor of linear perturbations normalized so that  $b = 1$  at  $z = 0$ , and  $W(k; M)$  is the Fourier-space representation of a real-space top-hat filter enclosing mass  $M$  at the mean density of the universe.

We define the mass function  $f(\sigma, z; X)$  through:

$$f(\sigma, z; X) \equiv \frac{M}{\rho_0} \frac{dn_X(M, z)}{d \ln \sigma^{-1}}, \quad (4)$$

where  $X$  is a label identifying the cosmological model and halo finder under consideration,  $n(M, z)$  is the abundance of haloes with mass less than  $M$  at redshift  $z$ , and  $\rho_0(z)$  is the mean density of the universe at that time.

The advantage of using  $\ln \sigma^{-1}$  as the mass variable is most evident when we consider the analytic models to which we compare. As we will see below, the Press–Schechter model predicts a simple analytic form for  $f(\sigma, z)$  which has no explicit dependence on redshift, power spectrum or cosmological parameters; a single mass function describes structure in all Gaussian hierarchical clustering models at all times in any cosmology provided abundances are plotted in the  $f$ – $\ln(\delta_c/\sigma)$  plane, where  $\delta_c$  is a threshold parameter, possibly dependent on  $\Omega$ , which we discuss later. This very simple structure carries over to extensions of the Press–Schechter analysis such as that presented by Sheth et al. (1999). For a power-law linear power spectrum and  $\Omega = 1$ , clustering is expected to be self-similar in time on general grounds independent of the PS model (e.g. Efstathiou et al. 1988; Lacey & Cole 1994), implying again that mass functions at different times should map on to a unique curve in the  $f$ – $\ln \sigma^{-1}$  plane (although this curve could be a function of the power-law spectral index). For CDM power spectra, the spectral index varies quite weakly with scale so one might expect at most a weak dependence on redshift in this plane. At worst, use of  $\ln \sigma^{-1}(M)$  as the ‘mass’ variable ‘factors out’ most of the difference in the mass functions between different epochs, cosmologies and power spectra, and so allows a wider comparison, both among our own simulations and between these and those by other authors.

In Section 4.1, we describe the two analytic models with which we compare explicitly our numerical results in Section 4.2.

##### 4.1 Analytic models

The Press–Schechter model (e.g. Press & Schechter 1974; Bond et al. 1991; Lacey & Cole 1993) predicts a mass function

given by:

$$f(\sigma; \text{PS}) = \sqrt{\frac{2}{\pi}} \frac{\delta_c}{\sigma} \exp\left(-\frac{\delta_c^2}{2\sigma^2}\right), \quad (5)$$

where  $\delta_c$  is a threshold parameter usually taken to be the extrapolated linear overdensity of a spherical perturbation at the time it collapses. In an Einstein–de Sitter cosmology  $\delta_c = 1.686$ . In other cosmologies  $\delta_c$  is sometimes assumed to be a weak function of  $\Omega$  and  $\Lambda$  (see e.g. Eke et al. 1996). The PS mass function has the normalization property:

$$\int_{-\infty}^{\infty} f(\sigma; \text{PS}) d \ln \sigma^{-1} = 1. \quad (6)$$

This implies that all of the dark matter is attached to haloes of some mass.

Sheth & Tormen (1999, hereafter ST) have introduced a new formula for the mass function (see their equation 10) which, for empirically determined choices of two parameters, gives a good fit to the mass functions measured in a subset of the  $N$ -body simulations analysed in this paper (the simulations ending in -gif in Tables 1 and 2). Their mass function can be expressed as:

$$f(\sigma; \text{ST}) = A \sqrt{\frac{2a}{\pi}} \left[ 1 + \left( \frac{\sigma^2}{a\delta_c^2} \right)^p \right] \frac{\delta_c}{\sigma} \exp\left(-\frac{a\delta_c^2}{2\sigma^2}\right), \quad (7)$$

where  $A = 0.3222$ ,  $a = 0.707$  and  $p = 0.3$ . Sheth et al. (1999, hereafter SMT) extended the excursion set derivation of the PS formula developed by Bond et al. (1991) to include an approximate treatment of ellipsoidal collapse, and showed this to produce a mass function almost identical in shape to equation (7). Their derivation forces this mass function to obey the integral relation of equation (6). Below, we compare their mass function with our  $N$ -body results, including mass-scales, redshifts and cosmologies other than those it was originally forced to fit. In a separate paper (Colberg et al. 2000), we compare the clustering of haloes in our Hubble volume simulations with the predictions of the SMT model.

Other analytic models for the halo mass function have been proposed recently by Monaco (1997a,b) and Lee & Shandarin (1998). These are substantially poorer fits to our data than the Sheth et al. (1999) model and we do not consider them further in this paper. Other published discussions of ‘Press–Schechter’ predictions have made use of filter functions other than the spherical top-hat, or have treated the threshold  $\delta_c$  as an adjustable parameter. We will not pursue the first of these possibilities at all, and we only deviate from standard assumptions about  $\delta_c$  in Section 5. There we show that taking  $\delta_c = 1.686$  in *all* cosmologies leads to excellent agreement with our numerical data if haloes are defined at fixed overdensity independent of  $\Omega$ , rather than at an  $\Omega$ -dependent overdensity as in the more conventional approach.

##### 4.2 Comparison to simulated mass functions

In order to make proper comparisons between analytic models and our simulated halo mass functions, we smooth the analytic predictions in the same way as we smoothed the simulation results in Section 3. In practice, this smoothing changes the predictions very little; the difference is only perceptible at high masses where the curves are very steep.

Interpolation formulae that accurately represent our (unsmoothed)

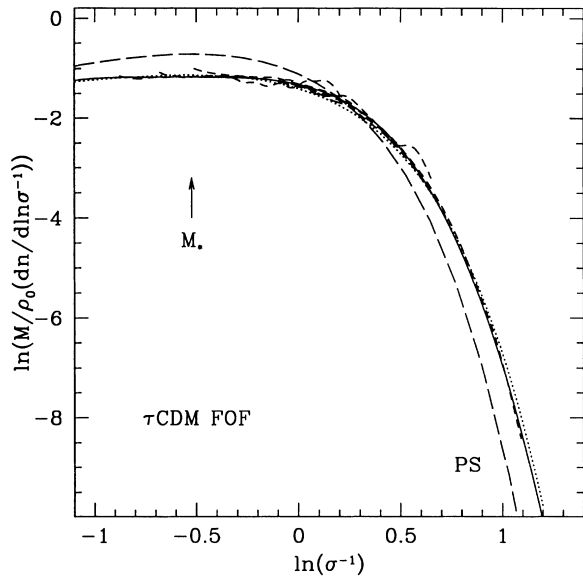


**Figure 3.** A comparison of analytic models with the halo mass function at  $z = 0$  in our  $N$ -body simulations of the  $\tau$ CDM cosmology. Haloes were found using the FOF algorithm with  $b = 0.2$ . The short dashed lines show results from the individual  $\tau$ CDM simulations used in this paper, the solid curve is the fit of equation (B1) to the combined results of the simulations, while the dashed line shows the PS prediction and the dotted line the ST prediction, both using  $\delta_c = 1.686$ . The arrow marks the characteristic mass-scale,  $M_*$ , where  $\sigma(M_*) = \delta_c$ , and corresponds to the position of the peak in the Press–Schechter mass multiplicity function. Note that we use natural logarithms in this plot.

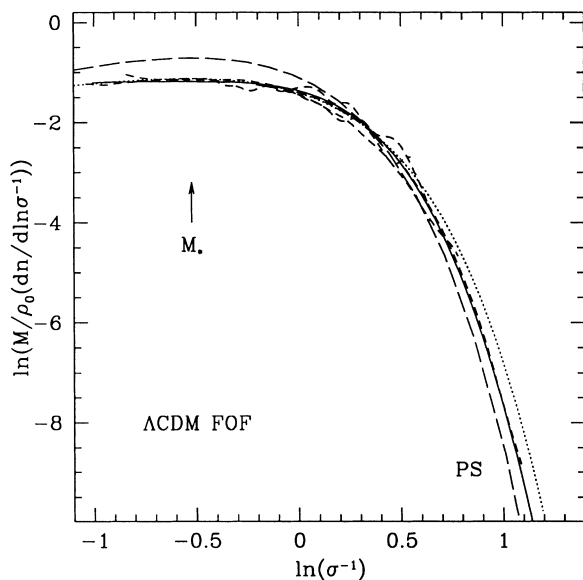


**Figure 4.** A comparison of analytic models with the halo mass function at  $z = 0$  in our  $N$ -body simulations of the  $\Lambda$ CDM cosmology. Haloes were found using the FOF algorithm with  $b = 0.164$ . The short dashed lines show results from the individual  $\Lambda$ CDM simulations used in this paper, the solid curve is the fit of equation (B2) to the combined results of the simulations, while the long dashed line shows the PS prediction and the dotted line the ST prediction, both using  $\delta_c = 1.675$ . The arrow marks the characteristic mass-scale,  $M_*$ , where  $\sigma(M_*) = \delta_c$ , and corresponds to the position of the peak in the Press–Schechter mass function. Note that we use natural logarithms in this plot.

mass functions are given in Appendix B and plotted (after smoothing) in Figs 3 and 4. Fig. 3 compares the FOF(0.2) halo mass function in the  $\tau$ CDM simulations with the PS and ST formulae assuming  $\delta_c = 1.686$ . At the high-mass end ( $\ln \sigma^{-1} > 0$ ), the simulation results lie well above the PS prediction. This discrepancy has been observed by a large number of authors (e.g. Efstathiou et al. 1988; White et al. 1993; Gross et al. 1998; Governato et al. 1999). Our simulations confirm that the divergence increases at even larger halo masses than those accessible to previous simulators. For  $\ln \sigma^{-1} < 0.3$ , the PS curve overestimates the simulated mass functions, and at the characteristic mass  $M_*$  (where  $\sigma = \delta_c$  and so  $\ln \sigma^{-1} = -0.52$ ), the halo abundance is only 60 per cent of the PS prediction. This conclusion agrees with the results of Efstathiou et al. (1988) and Gross et al. (1998) who found a similar discrepancy for a number of different cosmological models. Adjusting the simulated mass functions by altering halo finder parameters, or the analytic predictions by altering  $\delta_c$ , tends to shift the relevant curves in the  $\ln f - \ln \sigma^{-1}$  plane without much altering their shape. As a result, it does not significantly improve the overall agreement between the PS model and the numerical data.

By contrast, the ST mass functions give an excellent fit to the  $N$ -body results in Fig. 3. Good agreement is to be expected at the low-mass end since a subset of our simulation data was used by Sheth & Tormen (1999) to determine the parameters of their fitting function. This fitting function matches our numerical data for  $\tau$ CDM-FOF over their entire range, including large masses which were not considered in the original fit.

Fig. 4 shows the analogous comparison in the case of the  $\Lambda$ CDM model. Here, the FOF(0.164) halo mass function in the simulations is compared to the PS and ST predictions using  $\delta_c = 1.675$  as advocated by Eke et al. (1996) for this cosmology. With these choices of parameters, the PS curve gives a better fit to the simulated mass function at high masses than in the  $\tau$ CDM case, although it still underestimates the abundance of high-mass clusters and substantially overestimates the abundance near  $M_*$ . The ST model is a poorer fit to the numerical data than for  $\tau$ CDM, substantially overestimating abundances at high masses. However, as we will show in the next section, this disagreement is all but removed by different (and simpler) assumptions about the appropriate parameters for halo finders when  $\Omega < 1$ .

All the above comparisons refer to haloes identified using the FOF halo finder with standard parameters. We have checked that very similar results are obtained if haloes are identified using the SO halo finder, again with standard parameters. This similarity was previously noted by Tormen (1998).

It is interesting to compute the fraction of the total cosmic mass density that is included in haloes over the full range of validity of our simulation mass functions ( $\sim 3 \times 10^{11}$  to  $\sim 5 \times 10^{15} h^{-1} M_\odot$ ). Using our fits to the FOF data in Figs 3 and 4, we find this fraction to be 0.37 both in  $\tau$ CDM and in  $\Lambda$ CDM. The corresponding fraction for the PS mass function is 0.50. Where is the remaining mass? Clearly, higher-resolution simulations will show some proportion to be in haloes too small to have been resolved by our current simulations. However, there is no guarantee that such higher-resolution simulations will produce a total halo mass fraction that converges to unity. Much of the dark matter may not lie in haloes identified by an FOF(0.2) (or other) halo finder, but rather in a smooth, low-density component, perhaps in extensions of the identified haloes beyond their artificial  $b = 0.2$  boundaries. This possibility is suggested by the fact that our simulated mass functions remain low compared to the PS curve at the smallest

masses for which we can measure them. A straightforward extrapolation of our FOF(0.2) curves contains only  $\sim 70$  per cent of the total mass. Unfortunately, this extrapolation is not unique as shown by the fact that the ST mass function can fit all our numerical data and yet is normalized to give a total halo mass fraction of unity. More numerical data are needed to study the low-mass behaviour of the mass function in order to resolve this issue.

## 5 TOWARDS A GENERAL FITTING FORMULA

In this section, we first show that, when expressed in terms of  $\ln \sigma^{-1}$ , the mass functions in our two cosmological models vary only very little with redshift, or equivalently with the effective slope of the power spectrum. With our current definition of haloes, however, the mass functions in the  $\tau$ CDM and  $\Lambda$ CDM models are different. In Section 5.2, we show that this difference all but disappears if, instead of using a FOF linking length that varies with  $\Omega$ , we simply identify clusters with a constant linking length,  $b = 0.2$ , in both cosmologies. A general fitting formula can then accurately describe the halo mass function in a wide range of cosmological models.

### 5.1 Comparison of the mass function at different redshifts

For a scale-free power spectrum, the mass function expressed in terms of  $\ln \sigma^{-1}$  should be independent of redshift. Any differences must be due to Poisson sampling or to systematic errors introduced by numerical inaccuracies that break the scaling laws. For a CDM spectrum, for which the spectral slope is a function of scale, there could, in principle, be genuine evolution of the mass function but, if the amount of evolution is small, it may be masked by numerical effects.

In the  $\tau$ CDM model, a suitable rescaling of the length and mass units allows the mass function at non-zero redshift to be regarded as the redshift zero mass function of a simulation with a different power spectrum but identical normalization. Differences in the  $f$ - $\ln \sigma^{-1}$  plane between mass functions at different redshifts can therefore indicate a dependence of the mass function either on the shape of the power spectrum or on numerical effects. In order to exploit this regularity, and also to compare our results with those of Governato et al. (1999), we parametrize each simulation output by an effective power spectral slope  $n_{\text{eff}}$ ,

$$n_{\text{eff}} = 6 \frac{d \ln \sigma^{-1}}{d \ln M} - 3, \quad (8)$$

where we evaluate the derivative at the point where  $\sigma = 0.5$ , corresponding roughly to cluster scales for  $\Omega = 1$  and  $z = 0$ . For a scale-free power spectrum,  $n_{\text{eff}}$  is the power-law index in  $P(k) \propto k^n$ . We have calculated the FOF(0.2) mass function for the  $\tau$ CDM-hub simulation at redshifts  $z = 0.0, 0.18, 0.44$  and  $0.78$ , for which  $n_{\text{eff}} = -1.39, -1.48, -1.58$  and  $-1.70$  respectively. We can extend this range of spectral slopes by considering, in addition, the mass functions determined by Governato et al. (1999). Four outputs of their SCDM model correspond to  $\sigma_8 = 1.0, 0.7, 0.47$  and  $0.35$ , for which  $n_{\text{eff}} = -0.71, -0.90, -1.12$  and  $-1.28$  respectively. Thus, the two sets of simulations cover the range  $-0.71$  to  $-1.7$  in spectral slope but do not overlap.

Fig. 5 shows the mass functions determined from these two simulation sets. We stress that the present comparison supersedes

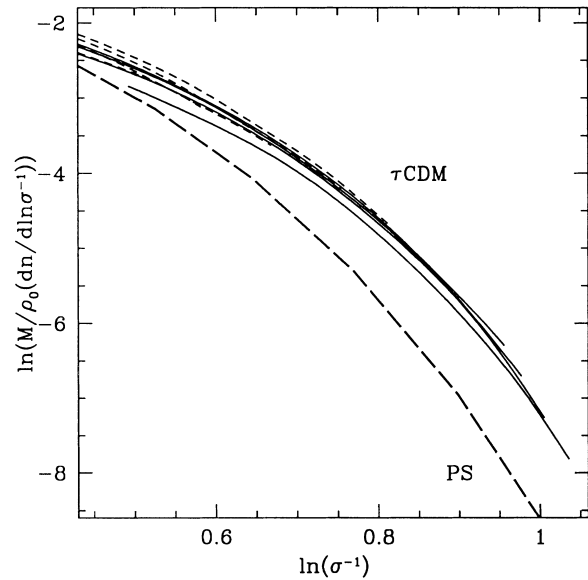


**Figure 5.** A comparison of mass functions in different simulations at different epochs. The full curves show the FOF(0.2) mass functions for the  $\tau$ CDM-hub simulation at redshifts  $z = 0, 0.18, 0.44$  and  $0.78$ . The dashed curves show the corresponding functions for the SCDM simulations of Governato et al. (1999) at four epochs for which  $\sigma_8 = 1.0, 0.7, 0.47$  and  $0.35$  respectively. The heavy dashed curve shows the PS model function. Both simulation data sets show a weak trend with  $\sigma_8$ , but the trends are opposite! See the text for discussion. Note that we use natural logarithms in this plot.

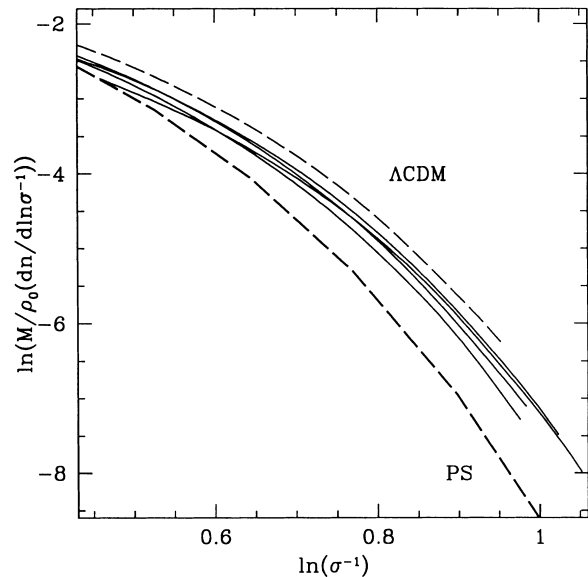


**Figure 6.** A comparison of mass functions in different simulations at different epochs. The full curves show the FOF mass function for the  $\Lambda$ CDM-hub simulation at redshifts  $z = 0, 0.27, 0.96$  and  $1.44$ . The first three form a sequence going from bottom to top, while the  $z = 1.44$  output is slightly lower than  $z = 0.96$ . The light dashed curve shows the  $\tau$ CDM-hub ( $z = 0$ ) mass function. The heavy dashed curve shows the PS theory model function. The trend with redshift is in the opposite direction to that in the  $\tau$ CDM model except at the highest redshift where the trend appears to reverse. The initial trend reflects the varying linking length used to define the haloes. For  $\tau$ CDM this choice was independent of redshift. Note that we use natural logarithms in this plot.

the preliminary comparison presented by Governato et al. (1999). The agreement between the various mass functions is good, with a variation of only 30 per cent over the range in  $n_{\text{eff}}$  from  $-0.7$  to  $-1.7$ . On closer inspection, the curves from the  $\tau$ CDM-hub simulation form a sequence in which the mass function decreases with increasing redshift (or with decreasing  $n_{\text{eff}}$ ) while the curves from Governato et al. (1999) also vary systematically, but in the opposite direction! The reason for these differing weak trends is unclear. They could reflect the differences in power spectrum shape between the two simulations, or perhaps small systematic numerical errors in one or both of them. (Note that, since the Hubble volume simulation follows a much larger volume than the simulation of Governato et al., its mass function is much better determined for large masses.) However, the magnitude of these trends (a total range below 30 per cent) is sufficiently small as to be of no real interest.

Fig. 6 shows mass functions at various epochs in the  $\Lambda$ CDM model. Here the curves are affected not only by the variation of spectral shape with redshift (as for  $\tau$ CDM) but also by the variation in the linking length which defines the simulated haloes. For this plot we chose to follow the relation proposed by Eke et al. (1996). The  $z = 0$  mass function (the lowest solid curve in the figure) is then significantly below the  $z = 0$   $\tau$ CDM mass function (the light dashed curve). Furthermore, in contrast to  $\tau$ CDM, the  $\Lambda$ CDM mass function initially moves upwards in the  $f\text{-}\ln\sigma^{-1}$  plane with increasing redshift. This can be attributed in large part

to the increasing linking length (see below). The upward trend reverses between  $z = 0.96$  and  $z = 1.44$ , perhaps reflecting the rapid convergence of  $\Omega$  and  $b/b$  to the  $\tau$ CDM values. As in the  $\tau$ CDM case, the differences are all rather small. We conclude that, although with the halo definition used in this section, the  $\tau$ CDM and  $\Lambda$ CDM mass functions are slightly different, there is no evidence for a significant systematic variation in the high-mass end of the mass function with redshift, with power spectrum slope  $n_{\text{eff}}$ , or with  $\Omega$ , once it is transformed to the appropriate variables.

## 5.2 A general fitting formula

The results of the last section suggest that it may be possible to find a universal formula that provides a reasonably accurate description of the halo mass function over a wide range of redshifts and in a wide range of cosmologies. Here, we show that a formula very similar to that suggested by ST is indeed successful if haloes are defined at the same overdensity at all times and in all cosmologies *independent of*  $\Omega$ . We concentrate on haloes defined using FOF(0.2), but have found very similar results using SO(180). Table 2 lists the simulation outputs used in this section. These include the data already analysed from our own simulations and those of Governato et al. (1999), together with additional data from the SCDM and OCDM (open with  $\Omega_0 = 0.3$ ) simulations in Jenkins et al. (1998). Because of the extended range of power

**Table 2.** Parameters of  $N$ -body simulations used in Figs 7, 8 and 9. Columns 2–5 give the cosmological parameters, and the normalization of the power spectrum at the present epoch. Columns 6 and 7 give the number of particles and the size of the simulation cubes. Column 8 gives the redshift of the output at which FOF groups were found, and column 9 gives the effective power spectrum slope at  $\sigma = 0.5$  defined by equation (8).

Simulation	$\Omega_0$	$\Lambda_0$	$\Gamma$	$\sigma_8$	$N_{\text{part}}$	$L_{\text{box}} (h^{-1} \text{Mpc})$	$z$	$n_{\text{eff}}$
$\tau$ CDM-gif	1.0	0.0	0.21	0.60	16 777 216	84.5	0.00	-1.39
$\tau$ CDM-gif	1.0	0.0	0.21	0.60	16 777 216	84.5	1.94	-1.96
$\tau$ CDM-gif	1.0	0.0	0.21	0.60	16 777 216	84.5	2.97	-2.13
$\tau$ CDM-gif	1.0	0.0	0.21	0.60	16 777 216	84.5	4.04	-2.26
$\tau$ CDM-int	1.0	0.0	0.21	0.60	16 777 216	160.3	0.00	-1.39
$\tau$ CDM-virgo	1.0	0.0	0.21	0.60	16 777 216	239.5	0.00	-1.39
$\tau$ CDM-512	1.0	0.0	0.21	0.51	134 217 728	320.7	0.00	-1.48
$\tau$ CDM-hub	1.0	0.0	0.21	0.60	1000 000 000	2000.0	0.00	-1.39
$\tau$ CDM-hub	1.0	0.0	0.21	0.60	1000 000 000	2000.0	0.18	-1.48
$\tau$ CDM-hub	1.0	0.0	0.21	0.60	1000 000 000	2000.0	0.44	-1.58
$\tau$ CDM-hub	1.0	0.0	0.21	0.60	1000 000 000	2000.0	0.78	-1.70
SCDM-gif	1.0	0.0	0.50	0.60	16 777 216	84.5	0.00	-0.99
SCDM-virgo	1.0	0.0	0.50	0.60	16 777 216	239.5	0.00	-1.08
$\Lambda$ CDM-gif	0.3	0.7	0.21	0.90	16 777 216	141.3	0.00	-1.17
$\Lambda$ CDM-gif	0.3	0.7	0.21	0.90	16 777 216	141.3	0.52	-1.32
$\Lambda$ CDM-gif	0.3	0.7	0.21	0.90	16 777 216	141.3	2.97	-1.72
$\Lambda$ CDM-gif	0.3	0.7	0.21	0.90	16 777 216	141.3	5.03	-2.00
$\Lambda$ CDM-512	1.0	0.0	0.21	0.90	134 217 728	479.0	0.00	-1.25
$\Lambda$ CDM-512	1.0	0.0	0.21	0.90	134 217 728	479.0	5.00	-2.08
$\Lambda$ CDM-hub	0.3	0.7	0.21	0.90	1000 000 000	3000.0	0.00	-1.25
$\Lambda$ CDM-hub	0.3	0.7	0.21	0.90	1000 000 000	3000.0	0.27	-1.32
$\Lambda$ CDM-hub	0.3	0.7	0.21	0.90	1000 000 000	3000.0	0.96	-1.51
$\Lambda$ CDM-hub	0.3	0.7	0.21	0.90	1000 000 000	3000.0	1.45	-1.62
OCDM-gif	0.3	0.0	0.21	0.85	16 777 216	141.3	0.00	-1.20
OCDM-virgo	0.3	0.0	0.21	0.85	16 777 216	239.5	0.00	-1.20
SCDM-gov	1.0	0.0	0.5	1.0	46 656 000	500.0	0.00	-0.71
SCDM-gov	1.0	0.0	0.5	1.0	46 656 000	500.0	0.43	-0.90
SCDM-gov	1.0	0.0	0.5	1.0	46 656 000	500.0	1.13	-1.12
SCDM-gov	1.0	0.0	0.5	1.0	46 656 000	500.0	1.85	-1.28

spectral shapes involved, we ‘deconvolve’ the smoothed mass functions by multiplying by  $\exp(-\alpha^2/59)$ , where  $\alpha$  is the local slope of  $\log_{10}(dn/d\log_{10}M)$  (see Section 3).

Fig. 7 shows all the data plotted on the  $f$ - $\ln\sigma^{-1}$  plane. As

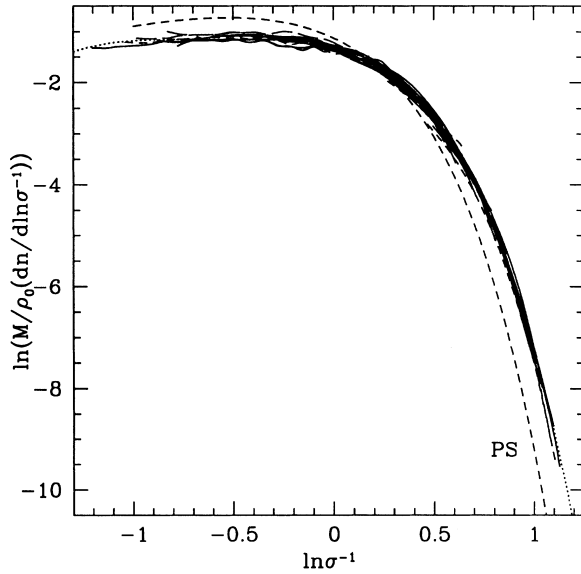


**Figure 7.** The FOF(0.2) mass functions of all the simulation outputs listed in Table 2. Remarkably, when a single linking length is used to identify haloes at all times and in all cosmologies, the mass function appears to be invariant in the  $f$ - $\ln\sigma^{-1}$  plane. A single formula (equation 9), shown with a dotted line, fits all the mass functions with an accuracy of better than about 20 per cent over the entire range. The dashed curve shows the Press–Schechter mass function for comparison.

before, all our curves are truncated at the mass corresponding to 20 particles (50 particles for the Governato et al. data) and where the Poisson error first exceeds 10 per cent. These curves encompass a wide range not only in  $\ln\sigma^{-1}$  but also in effective power spectrum slope,  $n_{\text{eff}}$ . Cosmic density ranges over  $0.3 \leq \Omega \leq 1.0$ . Remarkably, all curves lie very close to a single locus in the  $f$ - $\ln\sigma^{-1}$  plane. The use of a constant linking length has significantly reduced the amplitude of the redshift trend seen in the  $\Lambda$ CDM model in the previous section, and also places the OCDM outputs on the same locus.

The numerical data in Fig. 7 are well fitted by the following formula:

$$f(M) = 0.315 \exp(-|\ln\sigma^{-1} + 0.61|^{3.8}), \quad (9)$$

valid over the range  $-1.2 \leq \ln\sigma^{-1} \leq 1.05$ .

In Fig. 8 we plot the difference between the measured mass functions and our fitting formula. The fit is good to a fractional accuracy better than 20 per cent for  $-1.2 \leq \ln\sigma^{-1} \leq 1$ . This is a very significant improvement over the Press–Schechter formula, which would exceed the vertical limits of the plot! The curves for the open models with  $\Omega = 0.3$  are slightly high in this plot but only by  $\sim 10$  per cent. The spread between the different curves increases for large  $\ln\sigma^{-1}$ . This may simply reflect the fact that the very steep high-mass end of the mass function is sensitive to numerical effects which change the masses of clusters in a systematic way.

As shown in the figure, equation (9) is very close to the formula proposed by Sheth & Tormen (1999); there is a small difference in the high-mass tail, for  $\ln\sigma^{-1} > 0.9$ . A non-linear least-squares fit of equation (7) to the simulation data in Fig. 8 shows that the fit

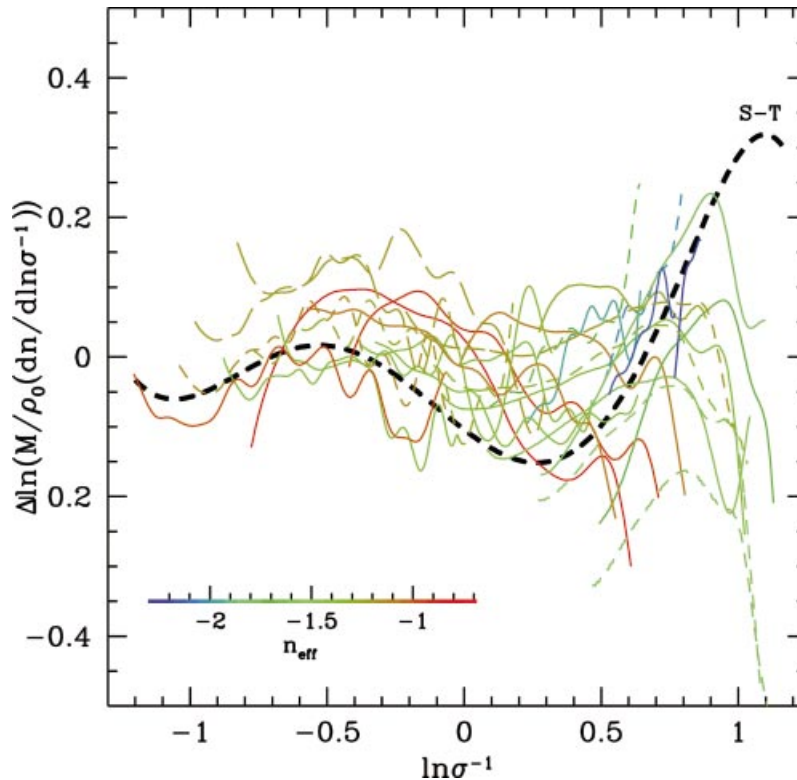


**Figure 8.** The residual between the fitting formula (equation 9) and the FOF(0.2) mass functions for all the simulation outputs listed in Table 2. The lines are colour coded according to the value of  $n_{\text{eff}}$ . Solid lines correspond to simulations with  $\Omega = 1$ , short dashed lines to flat low- $\Omega_0$  models, and long dashed lines to open models. The heavy dashed line shows the Sheth–Tormen formula (equation 7).

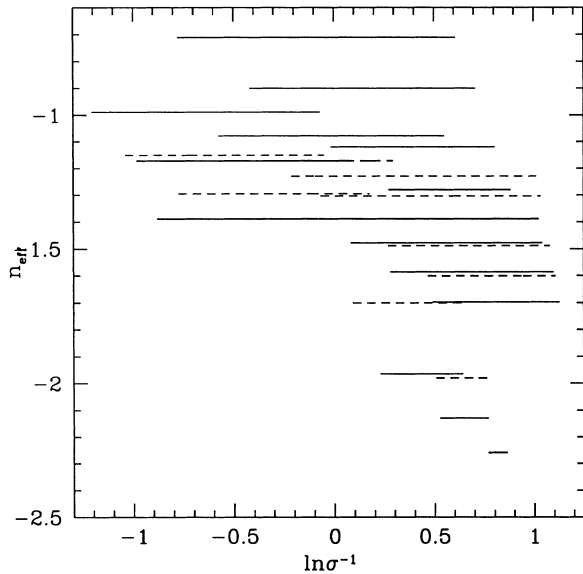


**Figure 9.** The parameter range covered by the simulation outputs listed in Table 2. The high-mass end of the mass function is well determined for a range of values of the parameter  $n_{\text{eff}}$ , while the low-mass end is only determined well for high values of  $n_{\text{eff}}$ . Dashed lines indicate models with  $\Omega_0 < 1$ .

can be improved by adjusting the parameters  $A$ ,  $p$  and  $a$ . If the normalization constraint, equation (6), is ignored, all three parameters can be allowed to vary freely. In this case, the best fit is obtained for  $A = 0.353$ ,  $p = 0.175$  and  $a = 0.73$  (and 0.84 of the mass is in haloes). If the normalization constraint is enforced, then only two parameters can vary; in this case the fit is not as good as that provided by equation (9).

Fig. 9 shows the area of the  $\ln \sigma^{-1}$ – $n_{\text{eff}}$  parameter space which is occupied by the data in Fig. 8. The high-mass end has good coverage in  $n_{\text{eff}}$  with values up to  $-2.3$ . In practice this means that, for currently popular cosmologies, the high-mass tail of the halo mass function is well determined at all redshifts where galaxies have so far been observed. The  $\tau$ CDM-gif simulation at  $z = 4.04$  has  $n_{\text{eff}} = -2.26$  and agrees well with  $\tau$ CDM-hub, which determines the high-mass end of the mass function at more recent epochs. We have checked that the  $\tau$ CDM-gif  $z = 5$  output, which has  $n_{\text{eff}} = -2.35$ , is also consistent with our fitting function, although its Poisson errors are slightly too large to satisfy our 10 per cent criterion for inclusion in Figs 7–9. For low  $\Omega$  our fitting formulae should work to even higher redshift. Since fluctuations grow more slowly for low  $\Omega$ , and the value of  $\sigma_8$  required to match current cluster abundances is higher, low-density cosmologies predict substantially less negative values for  $n_{\text{eff}}$  at each redshift.

## 6 CONCLUSIONS

We have derived halo mass functions at  $z = 0$  from simulations of the  $\tau$ CDM and  $\Lambda$ CDM cosmologies over more than four orders of magnitude in mass,  $\sim 3 \times 10^{11}$  to  $\sim 5 \times 10^{15} h^{-1} M_{\odot}$ . In particular, our two Hubble volume simulations provide the best available predictions for the abundance of the most massive clusters. We have checked the sensitivity of our mass functions to choice of group finder, to limiting overdensity and to numerical parameters such as softening, particle mass and starting redshift (see

Appendix A). Most dependences are weak. In particular, with a friends-of-friends group finder, the mass function is robustly determined with systematic uncertainties at or below the 10 per cent level for groups containing 20 particles or more. Somewhat higher particle numbers are needed for reliable results with a spherical overdensity group finder.

The mass functions we find for these two cosmologies, as well as for additional simulations of the SCDM and OCDM cosmologies, display the kind of universality predicted by the Press–Schechter model. When expressed in suitable variables, the mass function is independent of redshift, power spectrum shape,  $\Omega$  and  $\Lambda$ . This universality only obtains when we define haloes in our simulations at fixed overdensity *independent of*  $\Omega$ . When we use the spherical collapse model to define the appropriate overdensity, as suggested by Lacey & Cole (1994) and Eke et al. (1996), we find mass functions for low-density cosmologies which vary weakly but systematically with redshift. As has been noted before, the Press–Schechter model overestimates the abundance of  $M_*$  haloes and underestimates the abundance of massive haloes in all cosmologies. On the other hand, the fitting function proposed by Sheth & Tormen (1999) is a very good fit to the universal mass function we find, and is close to the best fit we give as equation (9). As shown by Sheth et al. (1999), this shape is a plausible consequence of extending the excursion set derivation of the PS model to include ellipsoidal collapse.

Our ‘universal’ mass function has considerable generality since the simulations cover a wide range of parameter space:  $\Omega$  in the range 0.3–1, effective spectral power index in the range  $-1$  to  $-2.5$ , and inverse fluctuation amplitude in the range  $-1.2 \leq \ln \sigma^{-1} \leq 1.05$ . For standard cosmologies this corresponds approximately to the mass range  $10^{11}$  to  $10^{16} h^{-1} M_{\odot}$  at  $z = 0$ , and to the high-mass tail of the mass function out to redshift 5 or more. More work is needed to check the abundances predicted for low-mass haloes, in particular to see whether all mass is predicted to be part of some halo, or whether some fraction makes up a truly diffuse medium.

Data for many of the simulations analysed in this paper, as well as cluster and galaxy catalogues created as part of other projects, are available from <http://www.mpa-garching.mpg/Virgo>.

Software to convert equation (9) into a mass function, for a given power spectrum is available on request from ARJ (A.R.Jenkins@durham.ac.uk).

## ACKNOWLEDGMENTS

The simulations discussed here were carried out as part of the Virgo consortium programme, on the Cray-T3D/Es at the Edinburgh Parallel Computing Centre and the Rechenzentrum, Garching. We thank Fabio Governato for supplying the halo catalogues for the simulation of Governato et al. (1999). This work was supported by the EC network for ‘Galaxy Formation and Evolution’ and NATO CRG 970081 and by PPARC. CSF acknowledges a PPARC Senior Research Fellowship and a Leverhume Research Fellowship. SC acknowledges a PPARC advanced fellowship.

We thank the referee for his constructive comments on the manuscript.

## REFERENCES

- Bahcall N., Fan X., 1998, ApJ, 504, 1
- Bartelmann M., Huss A., Colberg J. M., Jenkins A., Pearce F. R., 1998, A&A, 330, 1

- Blanchard A., Bartlett J. G., 1998, *A&A*, 332, L49  
 Bond J. R., Efstathiou G., 1984, *ApJ*, 285, L45  
 Bond J. R., Cole S., Efstathiou G., Kaiser N., 1991, *ApJ*, 379, 440  
 Bower R. G., 1991, *MNRAS*, 248, 332  
 Burles S., Tytler D., 1998, *ApJ*, 507, 732  
 Colberg J. et al., 2000, *MNRAS*, 319, 209  
 Davis M., Efstathiou G., Frenk C. S., White S. D. M., 1985, *ApJ*, 292, 371  
 Efstathiou G., Rees M. J., 1988, *MNRAS*, 230, 5P  
 Efstathiou G., Frenk C. S., White S. D. M., Davis M., 1988, *MNRAS*, 235, 715  
 Eke V. R., Cole S., Frenk C. S., 1996, *MNRAS*, 282, 263  
 Eke V. R., Cole S., Frenk C. S., Henry P., 1998, *MNRAS*, 298, 1145  
 Evrard A. E. et al., 2000, 319, 209  
 Falco E. E., Kochanek C. S., Munoz J. A., 1998, *ApJ*, 494, 47  
 Governato F., Babul A., Quinn T., Tozzi P., Baugh C. M., Katz N., Lake G., 1999, *MNRAS*, 307, 949  
 Gross M. A. K., Somerville R. S., Primack J. R., Holtzman J., Klypin A., 1998, *MNRAS*, 301, 81  
 Henry P., 1997, *ApJ*, 489, L1  
 Jenkins A. et al., 1998, *ApJ*, 499, 20  
 Klypin A., Kravtsov A. V., Valenzuela O., Prada F., 1999, *ApJ*, 522, 82  
 Lacey C., Cole S., 1993, *MNRAS*, 262, 627  
 Lacey C., Cole S., 1994, *MNRAS*, 271, 676  
 Lee J., Shandarin S., 1998, *ApJ*, 500, 14  
 Monaco P., 1997a, *MNRAS*, 287, 753  
 Monaco P., 1997b, *MNRAS*, 290, 439  
 Moore B., Ghigna S., Governato F., Lake G., Quinn T., Stadel J., Tozzi P., 1999, *ApJ*, 524, 19  
 Press W. H., Schechter P., 1974, *ApJ*, 187, 425 (PS)  
 Ratra B., Sugiyama N., Banday A. J., Gorski K. M., 1997, *ApJ*, 481, 22  
 Seljak U., Zaldarriaga M., 1996, *ApJ*, 469, 437  
 Sheth R. K., Tormen G., 1999, *MNRAS*, 308, 119 (ST)  
 Sheth R. K., Mo H. J., Tormen G., 2001, *MNRAS*, in press  
 Somerville R. S., Primack J. R., 1999, *MNRAS*, 310, 1087  
 Tormen G., 1998, *MNRAS*, 297, 648  
 Viana P. T. P., Liddle A. R., 1996, *MNRAS*, 281, 323  
 White S. D. M., Rees M. J., 1978, *MNRAS*, 183, 341  
 White S. D. M., Efstathiou G., Frenk C. S., 1993, *MNRAS*, 262, 1023

## APPENDIX A: A RESOLUTION STUDY

To investigate the effects of mass resolution, gravitational softening and starting redshift, we carried out the three test simulations detailed at the bottom of Table 1. These simulations are all of an identically sized region,  $200 h^{-1}$  Mpc on a side, and are set up so that corresponding waves have identical phases and amplitudes in all three cases. Two of the simulations,  $\tau$ CDM-test1 and  $\tau$ CDM-test2, have the same particle mass as the Hubble volume simulation. The former has essentially identical numerical parameters to the  $\tau$ CDM-hub simulation, while the latter differs in having a smaller gravitational softening length. The  $\tau$ CDM-test3 simulation has eight times as many particles as  $\tau$ CDM-test1, but is otherwise identical. As a check of the effect of the starting redshift we repeated  $\tau$ CDM-test1 a second time but starting at redshift 14 rather than 29 (as for the other tests and  $\tau$ CDM-hub).

Fig. A1 shows the mass functions for haloes found with the FOF group finder using three different linking lengths ( $b = 0.1, 0.15$  and  $0.2$ ), for  $\tau$ CDM-test1 and  $\tau$ CDM-test3. Consistent with the results of Section 3, the FOF mass function is only very weakly dependent on the particle mass. Changing the softening makes an even smaller difference and we do not plot the curve for  $\tau$ CDM-test2; the average rms difference between the mass functions with 30 and  $100 h^{-1}$  kpc gravitational softening is just 0.0135 dex. If the softening were increased significantly beyond

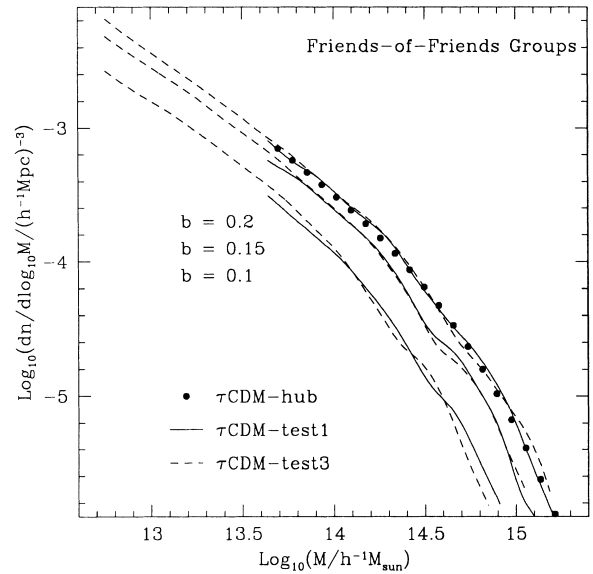


**Figure A1.** A resolution study of the effect of varying the particle mass on the mass function of FOF haloes for three values of the linking parameter,  $b$ . The dashed lines show the mass functions obtained from  $\tau$ CDM-test3, and the solid lines from  $\tau$ CDM-test1. These simulations have the same phases but differ by a factor of 8 in particle mass. The mass function is plotted for haloes with 20 particles and above. The filled circles show the corresponding mass function in  $\tau$ CDM-hub, which has the same particle mass as  $\tau$ CDM-test1. Defined in this way, the mass function is remarkably robust.

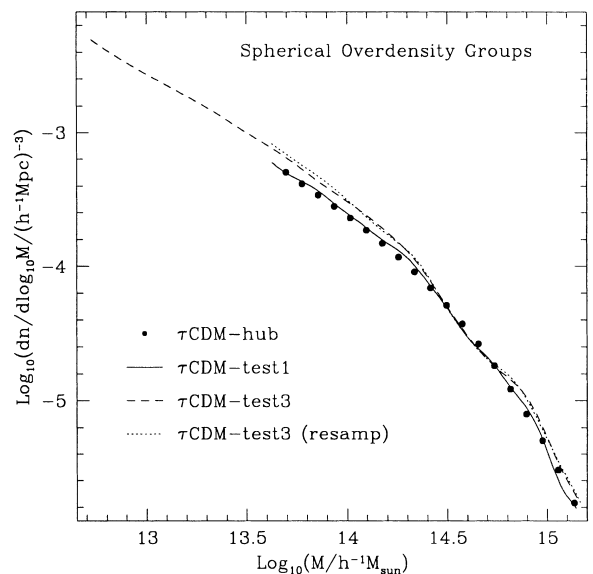


**Figure A2.** A resolution study of the effect of varying the particle mass on the mass function of SO haloes. The dashed line shows the mass function obtained from  $\tau$ CDM-test3, and the solid line from  $\tau$ CDM-test1. These simulations have the same phases but differ by a factor of 8 in particle mass. The mass function is plotted for haloes with 20 particles and above. The filled circles show the corresponding mass function in  $\tau$ CDM-hub, which has the same particle mass as  $\tau$ CDM-test1. The dotted line shows the SO mass function when one-in-eight particles are randomly sampled from  $\tau$ CDM-test3. This test shows that the SO mass function is sensitive to the particle mass, unlike the FOF mass function in Fig. A1.

$100 h^{-1}$  kpc, then we would expect the mass function to decrease as haloes become more and more diffuse. The mass function for  $\tau$ CDM-hub is shown also and agrees well with  $\tau$ CDM-test1, as it should. We conclude that the mass function of FOF haloes is remarkably robust to the numerical parameters in the simulations.

When haloes are identified using the SO group finder, the situation is slightly different. As Fig. A2 shows, the SO mass function from  $\tau$ CDM-test1 agrees well with that in  $\tau$ CDM-hub over the corresponding range of masses. Changing the softening to  $30 h^{-1}$  kpc in  $\tau$ CDM-test2 does not change the mass function much. However, changing the mass resolution by a factor of 8, as in  $\tau$ CDM-test3, leads to a significant change in the mass function at the low-mass end, which is now much closer to that determined from  $\tau$ CDM-virgo, a simulation with similar mass resolution. Resampling the high-mass resolution simulation,  $\tau$ CDM-test3, at random, at a rate of one-in-eight, does not have any noticeable effect on the mass function. This suggests that the resolution dependence of the mass function close to the resolution limit is not due simply to details of the cluster-finding algorithm (such as the position of the halo centre). Rather, it suggests that the difference may reflect genuine differences in the structural properties of marginally resolved haloes in simulations with different particle numbers.

The mass function is not very sensitive to the starting redshift unless this is so low that the neighbouring Zel'dovich displacements are so large as to interfere with the formation of the first non-linear objects. In practice, all the simulations compiled here pass this test easily. As a additional check, we repeated  $\tau$ CDM-test1, starting at  $z = 14$ . This made very little difference to the mass function overall, causing an rms average difference over the measured mass function of only 0.02 dex.

In summary, our tests indicate that we can derive an accurate mass function for FOF groups from the Virgo simulations (including the Hubble volume). The mass functions agree well in the overlap regions of simulations of different mass resolution even when haloes with only 20 particles per group are included. Perhaps surprisingly, the mass functions of SO groups do not match up nearly as well at such low particle numbers. A minimum of  $\sim 100$  particles is required to provide reasonable agreement in the overlap regions in this case.

## APPENDIX B: FITTING FORMULAE FOR THE FOF AND SO MASS FUNCTIONS

Here, we give fitting formulae for the (unsmoothed) mass functions of FOF and SO haloes, using the standard values of the group-finding parameters given in Section 2. These fits are plotted in Figs 3 and 4 of Section 4.

### 1. The friends-of-friends (FOF) group finder:

$\tau$ CDM/FOF(0.2) :

$$f(M) = 0.307 \exp(-|\ln \sigma^{-1} + 0.61|^{3.82}), \quad (\text{B1})$$

in the range  $-0.9 \leq \ln \sigma^{-1} \leq 1.0$ .

$\Lambda$ CDM/FOF(0.164) :

$$f(M) = 0.301 \exp(-|\ln \sigma^{-1} + 0.64|^{3.88}), \quad (\text{B2})$$

in the range  $-0.96 \leq \ln \sigma^{-1} \leq 1.0$ . The difference between these fitting functions and the actual mass functions is typically less than 10 per cent.

### 2. The spherical overdensity (SO) group finder:

$\tau$ CDM/SO(180) :

$$f(M) = 0.301 \exp(-|\ln \sigma^{-1} + 0.64|^{3.82}), \quad (\text{B3})$$

in the range  $-0.5 \leq \ln \sigma^{-1} \leq 1.0$ .

$\Lambda$ CDM/SO(324) :

$$f(M) = 0.316 \exp(-|\ln \sigma^{-1} + 0.67|^{3.82}), \quad (\text{B4})$$

in the range  $-0.7 \leq \ln \sigma^{-1} \leq 1.0$ . As discussed earlier, the differences between the SO mass functions are larger than for FOF haloes. Differences between the fit and the mass functions within the quoted mass range can be as large as 20 per cent.

Fig. B1 shows the residuals between the four fitting formulae quoted above and the mass functions in the simulations. Also shown are the differences between our fitting formulae and both the PS and ST models. The simulation curves are truncated at the high-mass end at the point where the fractional rms Poisson error reaches 10 per cent. The simulation mass functions may be seen to be consistent with one another at a level of about 10 per cent. As seen in previous plots, the PS curve is too high at low masses (low  $\ln \sigma^{-1}$ ) and too low at high masses. For the fit proposed by Sheth & Tormen (1999, equation 10) good agreement is to be expected at the low-mass end since a subset of the simulation data used here (the -gif simulations) was used by Sheth & Tormen (1999). Although their mass function is normalized (so that all the mass is attached to haloes), it does match our fits for  $\tau$ CDM-FOF rather well over their entire range. For the other models, the Sheth–Tormen fit overestimates the number of very massive clusters. Because of the normalization constraint, the Sheth–Tormen mass function exceeds the PS predictions for extremely low-mass haloes but this occurs at a point well beyond what can be tested easily in  $N$ -body simulations. Whether such low-mass behaviour is correct remains to be determined.

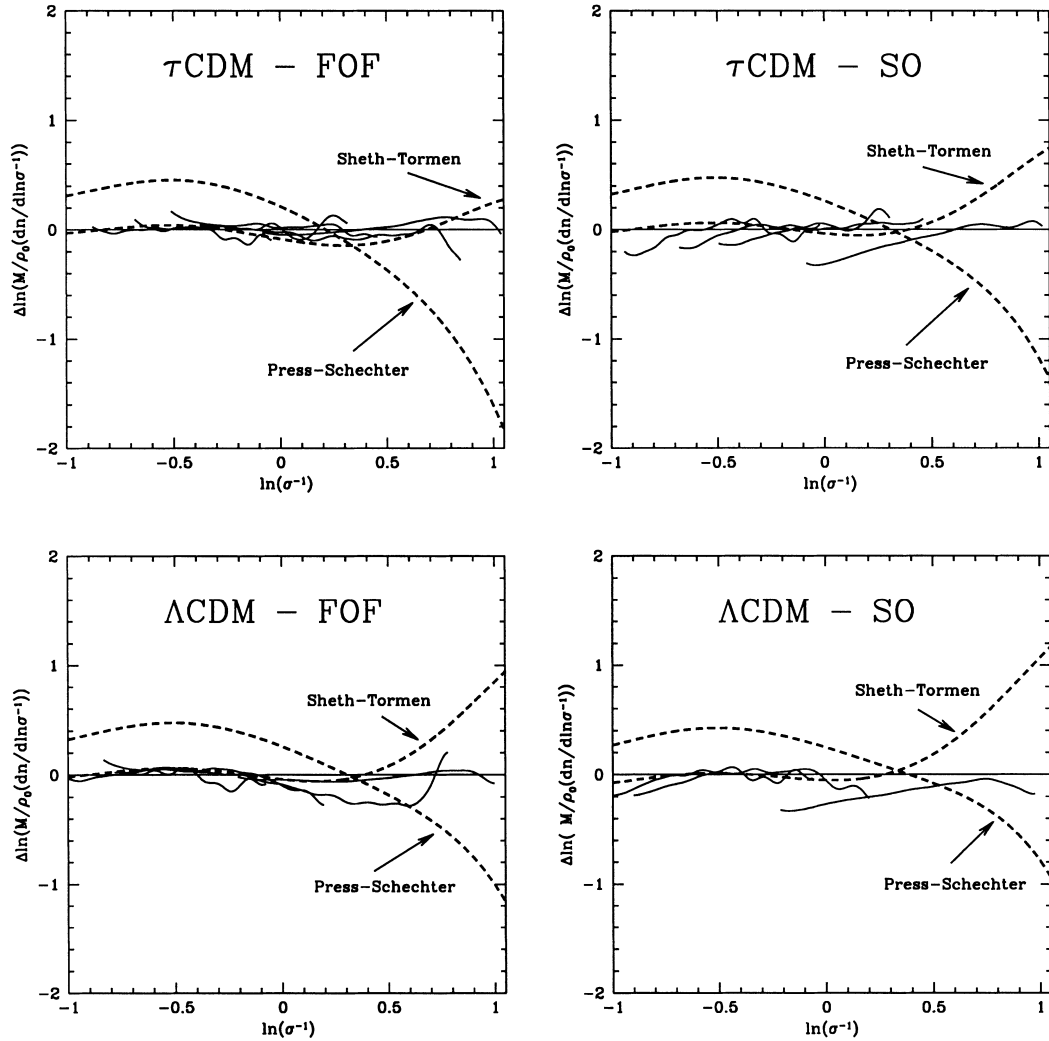


**Figure B1.** The residuals between the fitting formulae for the mass function given in Appendix B and (i) the simulations (solid lines) and (ii) the Press–Schechter and Sheth–Tormen models (dashed lines.) The simulation curves are plotted up to the point where the fractional Poisson error reaches 10 per cent. The simulations themselves can be seen to be mutually consistent at about the 10 per cent level although the differences are, for the most part, larger than the Poisson errors. The PS curve shows an excess at low masses and a deficit at high masses. The Sheth–Tormen mass function fits the low-mass end well, but overestimates the number of high-mass clusters. Note that we use natural logarithms in this plot.

This paper has been typeset from a  $\text{\TeX}/\text{\LaTeX}$  file prepared by the author.